



**HAL**  
open science

## Morphology control of self-organised Sr<sub>3</sub>V<sub>2</sub>O<sub>8</sub> nanostructures on SrVO<sub>3</sub> grown onto single and poly-crystalline subjacent SrTiO<sub>3</sub> substrates

B. Bérini, M. Dallochio, A. David, U. Luders, Bourlier Yoan, L. Rault, Rosine Coq Germanicus, Wilfrid Prellier, Y. Dumont, Valérie Demange, et al.

### ► To cite this version:

B. Bérini, M. Dallochio, A. David, U. Luders, Bourlier Yoan, et al.. Morphology control of self-organised Sr<sub>3</sub>V<sub>2</sub>O<sub>8</sub> nanostructures on SrVO<sub>3</sub> grown onto single and poly-crystalline subjacent SrTiO<sub>3</sub> substrates. Applied Surface Science, 2021, 566, pp.150759. 10.1016/j.apsusc.2021.150759 . hal-03335293

**HAL Id: hal-03335293**

**<https://hal.science/hal-03335293>**

Submitted on 15 Sep 2021

**HAL** is a multi-disciplinary open access archive for the deposit and dissemination of scientific research documents, whether they are published or not. The documents may come from teaching and research institutions in France or abroad, or from public or private research centers.

L'archive ouverte pluridisciplinaire **HAL**, est destinée au dépôt et à la diffusion de documents scientifiques de niveau recherche, publiés ou non, émanant des établissements d'enseignement et de recherche français ou étrangers, des laboratoires publics ou privés.

# Morphology control of self-organised Sr<sub>3</sub>V<sub>2</sub>O<sub>8</sub> nanostructures on SrVO<sub>3</sub> grown onto single and poly-crystalline subjacent SrTiO<sub>3</sub> substrates

Bruno Bérini<sup>1,\*</sup>, Marie Dallochio<sup>2</sup>, Adrian David<sup>2</sup>, Ulrike Lüders<sup>2</sup>, Yoan Bourlier<sup>1</sup>, Ludivine Rault<sup>3</sup>, Rosine Coq Germanicus<sup>2</sup>, Wilfrid Prellier<sup>2</sup>, Yves Dumont<sup>1</sup>, Valérie Demange<sup>3,\*</sup> and Arnaud Fouchet<sup>2,\*</sup>

<sup>1</sup> Université Paris-Saclay, UVSQ, CNRS, GEMaC, 45 avenue des Etats-Unis, 78035, Versailles, France


<sup>2</sup> Normandie Univ, ENSICAEN, UNICAEN, CNRS, CRISMAT, 14000 Caen, France

<sup>3</sup> Univ Rennes, CNRS, ISCR – UMR 6226, ScanMAT – UMS 2001, F-35000 Rennes, France

**Keywords:** SrVO<sub>3</sub> (SVO), strontium vanadate, transparent conducting oxide, combinatorial substrate epitaxy (CSE), nanostructure (NS)

## Corresponding authors


Dr. Bruno Bérini ; Université Paris-Saclay, UVSQ, CNRS, GEMaC, 45 avenue des Etats-Unis, 78035, Versailles, France.

 [orcid.org/0000-0002-9063-5194](https://orcid.org/0000-0002-9063-5194) – Email : [bruno.berini@uvsq.fr](mailto:bruno.berini@uvsq.fr)

Dr. Valérie Demange ; Université Rennes, CNRS, ISCR – UMR 6226, ScanMAT – UMS 2001, F-35000 Rennes, France.

 [orcid.org/0000-0002-8153-2660](https://orcid.org/0000-0002-8153-2660) – Email : [valerie.demange@univ-rennes1.fr](mailto:valerie.demange@univ-rennes1.fr)

Dr. Arnaud Fouchet ; Normandie Université, ENSICAEN, UNICAEN, CNRS, CRISMAT, 14000 Caen, France.

 [orcid.org/0000-0002-3604-4756](https://orcid.org/0000-0002-3604-4756) – Email : [arnaud.fouchet@ensicaen.fr](mailto:arnaud.fouchet@ensicaen.fr)

## Abstract:

SrVO<sub>3</sub> (SVO) is a complex oxide with interesting optical and conduction properties as an indium-free transparent conducting oxide for electrode applications. In this paper, we report how the surface of SVO can be designed at the nanoscale from self-organized Sr<sub>3</sub>V<sub>2</sub>O<sub>8</sub> nanostructures (NS) with different shapes and morphologies depending on crystalline orientations. By combining transmission electron microscopy (TEM) and atomic force microscopy (AFM), we compare the characteristics of the NS for SVO films grown on SrTiO<sub>3</sub> (STO) polycrystalline substrates, according to combinatorial substrate epitaxy (CSE), with those of NS observed from SVO films deposited on STO single crystalline substrates with different crystallographic orientations ((100), (110), (111)). We are able not only to show that the obtained morphologies are correlated to the specific substrate orientation due to the epitaxial relationships between the NS, the SVO, and the substrate, but also to establish a NS library and determine the necessary crystalline orientations for a certain NS morphology on demand. Finally, dissolution of the NS in water leads to typical inverse imprints on the surface of the film, offering a fast and easy way to pattern the electrodes. This work presents a new way of patterning surfaces with a specific design of self-organized NS.

## Introduction

Ternary oxides (ABO<sub>3</sub>) with perovskite structure form a class of materials rich of various functional properties (piezoelectricity, ferroelectricity, superconductivity, etc.)<sup>1-5</sup>. This diversity is due to the wide range of cation sizes and the electronic filling of the *d* orbitals possible to be accommodated in the perovskite structure, which both modify their crystalline structure and the electronic properties. For example, by substituting the cation X (X: Ti, V) in the formula SrXO<sub>3</sub>, we obtain respectively SrTiO<sub>3</sub> (STO with 3*d*<sup>0</sup>) which is insulator and frequently used as substrate for all-oxides heterostructures<sup>4</sup> and SrVO<sub>3-δ</sub> (SVO with 3*d*<sup>1-δ</sup>) which is a metal and can be used as an electrode for integration of functional oxides<sup>6-8</sup>. This metallic behavior is also associated to a high optical transparency in the visible range due to electronic correlations, which makes SVO interesting as a new transparent conductor oxide<sup>9-13</sup>. Interestingly, both of these materials possess the same primitive cubic structure (space group *Pm* $\bar{3}$ *m*, N<sup>o</sup>221) with lattice constant *a* = 3.905 Å<sup>14</sup> (STO) and 3.843 Å for δ = 0 and 3.856 Å for δ = 0.1 (SVO)<sup>15-18</sup>, respectively. The similar lattice parameter in these compounds allows the vertical integration of the perovskite family through epitaxy<sup>19,20-22</sup>.

1  
2  
3  
4  
5  
6  
7  
8  
9  
10  
11  
12  
13  
14  
15  
16  
17  
18  
19  
20  
21  
22  
23  
24  
25  
26  
SVO is usually grown at low oxygen pressure to stabilize the  $V^{4+}$  state since vanadium is highly sensitive and more stable in the  $V^{5+}$  state ( $3d^0$ ). Therefore, films are typically grown under vacuum or in a low  $O_2$  partial pressure (less than  $1.2 \times 10^{-4}$  Pa at  $750^\circ\text{C}$ ) and rapidly cooled under vacuum to avoid the appearance of higher vanadium valence state phases such as insulating  $Sr_3V_2O_8$ . This phase appears in the form of elongated nanostructures (NS)<sup>23,24,10</sup>, with an epitaxial relationship to the SVO matrix, as it was shown in the case of (100)-oriented SVO films<sup>25,26</sup>. Furthermore, the NS have the particularity to grow also inside the SVO matrix, i.e. the NS are half buried down to the SVO film surface. Interestingly, the NS phase is highly soluble in water, leaving after dissolution imprints with a depth from 10 to 20 nm equal to their initial heights, building a network which can be useful for nano-patterning<sup>27</sup>. Therefore, nano-patterned electrodes can be developed for the integration of complex oxides promoting the development of devices or sensors at the nanoscale. As a promising transparent conductive oxide (TCO), such particular SVO surface can also be tailored to obtain very high surface area in optical devices. Finally, nanostructured surfaces can be used for different applications such as optical anti-reflective applications<sup>28</sup> or surface nano-structure-wettability<sup>29</sup>.

27  
28  
29  
30  
31  
32  
33  
34  
35  
36  
37  
38  
39  
40  
41  
42  
43  
44  
45  
46  
47  
48  
49  
50  
51  
52  
53  
54  
55  
56  
57  
58  
59  
60  
61  
62  
63  
64  
65  
Up to now, only elongated NS with two variants being oriented by  $90^\circ$  have been reported for SVO. Nevertheless, it would be useful to obtain different NS shapes, sizes and spatial distributions, in order to create other patterns which can be adaptable on request. As the NS are epitaxially grown on SVO, their characteristics and epitaxial relations should be related to the lattice misfit with respect to the SVO matrix. So the crystalline orientation of the SVO matrix becomes an important lever for the diversification of the NS shapes. In this study, we use polycrystalline substrates based on the combinatorial substrate epitaxy (CSE) approach in order to provide a full investigation of the different NS which can be obtained based on the crystalline orientations of the SVO matrix. In those polycrystalline substrates, each grain acts as a single crystal for the growth of the thin film<sup>30-37</sup>, so that all crystalline orientations of the SVO film can be obtained with only one substrate. These substrates can be synthesized from exotic materials with different structures not commercially available<sup>30,31,35</sup>. In the case of STO, atomically flat surfaces can be obtained<sup>36</sup> and also that the size of each grains can be tuned from 1 to  $40 \mu\text{m}$  depending on the annealing process. Additionally to low production costs compared to single crystalline substrates, these substrates may provide also the possibility of engineering physical properties of thin films via grain boundaries, in order to improve the thermoelectric<sup>37</sup> or magnetotransport properties, for example.

1  
2  
3  
4  
5  
6  
7  
8  
9  
10  
11  
12  
13  
14  
15  
16  
17  
18  
19  
20  
21  
22  
23  
24  
25  
26  
27  
28  
29  
30  
31  
32  
33  
34  
35  
36  
37  
38  
39  
40  
41  
42  
43  
44  
45  
46  
47  
48  
49  
50  
51  
52  
53  
54  
55  
56  
57  
58  
59  
60  
61  
62  
63  
64  
65

In this paper, SVO films are grown on commercially STO single crystalline substrates with the three available crystalline orientations (100), (110) and (111). Shapes and morphologies of the produced  $\text{Sr}_3\text{V}_2\text{O}_8$  surface NS are studied by transmission electron microscopy (TEM) and atomic force microscopy (AFM) relatively to their epitaxial relationship with respect to the SVO matrix orientation. Then, the use of CSE allows us to establish a complete library of the orientation-morphology relation of the NS<sup>36,38-40</sup>. This technique also reveals itself as a powerful tool to investigate the NS on the orientation of the SVO matrix underneath. Correlated to electron back scatter diffraction (EBSD) measurements, AFM imaging has been performed on selected grains to observe the morphologies and compare them to the three common orientations. Beyond these results, a “zoology” of these NS is presented, allowing to extract the necessary crystalline orientation from this library and adapt the NS shape and spatial orientation to the application requirements.

## Materials and methods

STO polycrystalline substrates were synthesized by mixing the two precursors  $\text{TiO}_2$  and  $\text{SrCO}_3$ <sup>36</sup>. After numerous machine and manual grinding steps, a calcination was performed at 1200 °C for 12 hours. After pressing, the pellets were sintered by spark plasma sintering (SPS) at 1500°C for 20 min in order to obtain a polycrystalline substrate with a grain size of around 40  $\mu\text{m}$ . The ceramic was then polished in order to obtain mirror-like surface for the local epitaxy of the SVO film. First, we use a manual process with several SiC papers (30-15-10-5  $\mu\text{m}$ ), then an automatic polishing (using a Struers polisher) with diamond liquid pastes (at 3  $\mu\text{m}$  and 1  $\mu\text{m}$  grain size) and the last step was a finishing process by  $\text{SiO}_2$ -colloidal solution.

Three commercial (SurfaceNet GmbH) STO (4x4x0.5  $\text{mm}^3$ ) substrates with the (100), (110) and (111) orientations were glued together with the polycrystalline STO substrate on the substrate holder with silver paste. The deposition of SVO films was performed at 850°C under  $2.5 \times 10^{-6}$  mbar of oxygen pressure using the pulsed laser deposition (PLD) technique. A KrF laser ( $\lambda = 248$  nm) at an energy of 1.85  $\text{J}/\text{cm}^2$  and repetition rate of 2 Hz was used. The base pressure of the chamber was  $5 \times 10^{-9}$  mbar and the distance between target and substrate approximately 5 cm. A 60-nm thick SVO film has been synthesized. After deposition, the samples were maintained 30 minutes at the growth temperature and oxygen partial pressure in order to form the NS, before being cooled down during 3 hours<sup>23</sup>.

1 The polycrystalline substrates were investigated by scanning electron microscopy (SEM) and  
2 EBSD, with a Zeiss Supra 55 instrument. The conditions for EBSD were: V = 15 kV, aperture  
3 = 60  $\mu\text{m}$  and working distance = 15 mm. Prior to deposition, the surfaces of the substrates were  
4 prepared by a  $\text{NH}_4\text{F}$  etching and an annealing at 950°C for 1 h. Figure SI-1 presents AFM  
5 images of a polycrystalline substrate for randomly selected areas after revealing terraces as  
6 presented in ref.<sup>36</sup>. Terraces are observed with dimensions related to the orientation of the  
7 different grains, which are randomly distributed.

13 Dissolution of the  $\text{Sr}_3\text{V}_2\text{O}_8$  NS was realized by rinsing the substrates under water for  
14 30 s, and before drying with  $\text{N}_2$ . To get a complete NS dissolution on the (111)STO substrate,  
15 a second irrigation with water for 30 s was used.

19 X-ray diffraction (XRD) analysis on the thin films was carried out using a  $\theta$ -2 $\theta$   
20 instrument (Bruker AXS D8 Advance) working with a monochromatized  $\text{Cu-K}\alpha 1$  radiation and  
21 equipped with a 1D detector (192 channels).

25 A Dimension ICON AFM (Bruker) has been used to observe morphology of NS present  
26 onto the surface of the various samples. The AFM topography measurements were performed  
27 in air with the PeakForce tapping mode. For this purpose, a silicon tip on nitride lever  
28 (ScanAsyst Air model, Bruker), with a 0.4 N/m spring constant and a nominal tip radius of 2  
29 nm was used with a resolution of 512 pixels  $\times$  512 pixels.

35 TEM study on the SVO films grown on (100), (110) and (111)STO was performed by  
36 using a Jeol 2100 instrument operating at 200 kV and equipped with a Gatan Orius 200D and a  
37 Gatan US Scan 1000 cameras. Samples for TEM were obtained by scratching the film with a  
38 diamond tip and the obtained fragments were collected on a commercial carbon-coated copper  
39 microgrid.

## 46 Results and discussion

### 48 1. $\text{Sr}_3\text{V}_2\text{O}_8$ nanostructures growth on single crystalline (100), (110) and (111)STO 50 substrates

53 Figure 1 shows the surface of SVO thin films simultaneously grown on three common  
54 orientations of STO. Comparable to what we previously observed for  $\text{CaVO}_3$ <sup>41</sup>, self-organized  
55  $\text{Sr}_3\text{V}_2\text{O}_8$  NS are observed in the analyzed regions of  $4 \times 4 \mu\text{m}^2$  with a morphology being function  
56 of the substrate orientation. On (100)STO, the surface presents elongated shapes of 160 nm  
57  
58  
59

1 length and 75 nm width with an average height of 25 nm (figure 1a). The root mean square  
2 roughness (RMS) of 6.8 nm is higher than the one given in ref.<sup>23</sup> due to a slight change in  
3 oxygen pressure during the growth and to an increased waiting time before cooling. The NS  
4 follow two perpendicular in-plane directions as already described in a previous study.<sup>24</sup> These  
5 Sr<sub>3</sub>V<sub>2</sub>O<sub>8</sub> NS with similar shape have also been reported on (100)NdGaO<sub>3</sub> (NGO) and  
6 (100)(LaAlO<sub>3</sub>)<sub>0.3</sub>(Sr<sub>2</sub>AlTaO<sub>6</sub>)<sub>0.7</sub> (LSAT) substrates<sup>11,42</sup>. Interestingly, on the (110)STO  
7 substrate, elongated NS can also be observed but they appear oriented along only one direction.  
8 The NS are a little longer than on (100)STO e.g. between 200 to 500 nm-long (figure 1b) and  
9 have a 16 nm-height. On (111)STO, two types of different NS appear: the first ones have  
10 triangular shape and the second ones are oblong NS as for (100)STO and (110)STO.  
11 Nevertheless, in this case, the oblong NS with variable size (50 to 250 nm) are oriented with an  
12 angle of 60° between them (figure 1c).  
13  
14  
15  
16  
17  
18  
19  
20  
21

22 Figure 2 displays XRD patterns of films grown on (100)-, (110)- and (111)STO substrates.  
23 These patterns exhibit only the substrate Bragg peaks and the 100, 110 and 111 reflections of  
24 the SVO phase, respectively, indicating that the substrates induce a preferential out-of-plane  
25 film orientation as expected for materials having the same structure type and similar lattice  
26 parameters. No secondary phases are found, neither peaks attributed to the Sr<sub>3</sub>V<sub>2</sub>O<sub>8</sub> NS due to  
27 a too small diffracting volume. The out-of-plane lattice constant of the SVO phase is  $a = 3.841$   
28 Å, 3.845 Å and 3.845 Å on (100)-, (110)- and (111)STO, respectively, close to the bulk values.  
29 To estimate the quality of our metallic samples, we use the residual resistivity ratio (RRR)<sup>8,11</sup>  
30 criteria, which is sensitive to defects as cation non-stoichiometry, oxygen deficiency or  
31 disorder, especially for SVO grown on STO substrates for which the lattice mismatch  $f$  is  
32 large<sup>10,11</sup> ( $f(\text{STO}) = +1,59\%$  is larger than  $f(\text{LAO}) = -1,37\%$ , larger than  $f(\text{LSAT}) = +0,65\%$ ,  
33 larger than  $f(\text{NGO}) = +0,52\%$ ). The following values of RRR were deduced from transport  
34 measurements in the range 2-300 K: 2.47 (STO100), 2.59 (STO110) and 2.73 (STO111),  
35 indicating a high quality of the SVO films on STO whatever their orientation.  
36  
37  
38  
39  
40  
41  
42  
43  
44  
45  
46  
47

48 In order to understand the different morphologies and shapes of the NS, we have  
49 investigated the epitaxial relationships between the NS and SVO by TEM measurements.  
50 Figure 3 displays electron diffraction patterns (EDP) of SVO films grown on the different STO  
51 substrates. For the film grown on (100)STO, EDP are taken along the [100] zone axis of the  
52 SVO phase. With the strong reflections of the SVO film, weak reflections from the two  
53 elongated Sr<sub>3</sub>V<sub>2</sub>O<sub>8</sub> variants are observed as depicted by the white square in the figure 3a. The  
54 intensity of these reflections is enhanced after a slight tilt of the sample (see figure 3b) and  
55  
56  
57  
58  
59  
60  
61  
62  
63  
64  
65

1 additional reflections, due to the double-diffraction phenomena between two phases having  
 2 symmetrical orientation relationship with respect to each other<sup>43</sup> appear. In previous studies,  
 3 the orientation of the NS was determined from indexation of these reflections as being  
 4  $[\bar{5}52]_{\text{Sr}_3\text{V}_2\text{O}_8}$  direction parallel to the  $[100]_{\text{SVO}}$  direction<sup>23,24</sup>. Comparison between pattern of  
 5  $\text{Sr}_3\text{V}_2\text{O}_8$  and that of SVO confirms the previously established epitaxial relationships between  
 6 the two vanadates<sup>23,24</sup>, which are  $[\bar{5}52]_{\text{Sr}_3\text{V}_2\text{O}_8} // [100]_{\text{SVO}}$ ,  $(110)_{\text{Sr}_3\text{V}_2\text{O}_8} // (011)_{\text{SVO}}$  and  
 7  $(\bar{1}\bar{1}\bar{5})_{\text{Sr}_3\text{V}_2\text{O}_8} // (01\bar{1})_{\text{SVO}}$ . The orientation of the  $\text{Sr}_3\text{V}_2\text{O}_8$  cell with respect to that of SVO is  
 8 schematized on the figure 4a. In this scheme, the coincidence lattice between both phases is  
 9 drawn by a red square. In particular, the  $d(110)_{\text{Sr}_3\text{V}_2\text{O}_8}$  inter-planar distance (2.81 Å) is close to  
 10 the  $d(110)_{\text{SVO}}$  and  $d(\bar{1}\bar{1}0)_{\text{SVO}}$  distances (2.71 Å) leading to two equiprobable possibilities for  
 11  $\text{Sr}_3\text{V}_2\text{O}_8$  to grow on SVO, *i.e.*  $(110)_{\text{Sr}_3\text{V}_2\text{O}_8} // (110)_{\text{SVO}}$  and  $(110)_{\text{Sr}_3\text{V}_2\text{O}_8} // (1\bar{1}0)_{\text{SVO}}$ , and  
 12 therefore to the formation of elongated NS 90° rotated with respect to each other. The  
 13 mismatches between SVO and  $\text{Sr}_3\text{V}_2\text{O}_8$  are equal to -3.69 % for one in-plane directions and -  
 14 14.39 % in the other one. In addition, high resolution TEM (HRTEM) was performed on the  
 15 SVO film. Figure SI-2a is a bright field image of an edge of a fragment showing NS which  
 16 partially extend underneath the  $(100)_{\text{SVO}}$  film. Therefore, HRTEM image of a NS without  
 17 subjacent SVO film is recordable in such area, as displayed on figure SI-2b. Fast Fourier  
 18 Transform (FFT) of this area shows a rectangular array corresponding to the  $[\bar{5}52]$  zone axis of  
 19 the  $\text{Sr}_3\text{V}_2\text{O}_8$  phase (figure SI-2c), while the FFT of the SVO film next to it shows a square  
 20 pattern. This result confirms the previously evidenced epitaxial relationship. The area where  
 21 the NS is lying on the perovskite displays a Moiré contrast due to the superposition of the  
 22 lattices and its FFT displays additional reflections due to these fringes (figure SI-2c). Similar  
 23 analysis was done for the film grown on  $(110)_{\text{STO}}$  (see figures 3c,d). A slight tilt of the  
 24  $[110]_{\text{SVO}}$  zone axis allows to see additional reflections due to the  $\text{Sr}_3\text{V}_2\text{O}_8$  NS, as depicted by  
 25 the square in figure 3c and magnified in the inset. Indexation of these reflections highlights that  
 26 the phase is oriented along the  $[5\bar{5}4]$  zone axis, as schematized on the figure 3d. The 110  
 27 reflections are in coincidence with the  $1\bar{1}0$  reflections of SVO, while the  $(2\bar{2}\bar{5})$  planes are  
 28 parallel to the  $(001)$  planes of SVO. The corresponding orientation of the  $\text{Sr}_3\text{V}_2\text{O}_8$  cell with  
 29 respect to that of the SVO cell is schematized in figure 4b. The mismatches between  $\text{Sr}_3\text{V}_2\text{O}_8$   
 30 and SVO are equal to -3.69 % for the first in-plane direction and -8.33% for the second one, if  
 31 the red subunit cells displayed in figure 4b are considered. The orientation of  $\text{Sr}_3\text{V}_2\text{O}_8$  with  
 32 respect to the SVO phase leads to the following epitaxial relationships between the two  
 33 vanadates:



$$[5\bar{5}4]\text{Sr}_3\text{V}_2\text{O}_8 // [110]\text{SVO}$$

$$(110)\text{Sr}_3\text{V}_2\text{O}_8 // (1\bar{1}0)\text{SVO}$$

$$(2\bar{2}\bar{5})\text{Sr}_3\text{V}_2\text{O}_8 // (001)\text{SVO}$$

Interestingly, as the in-plane directions of the (110)SVO are anisotropic, only one type of NS appears along the [110] in-plane direction compared to (100)SVO, which shows orthogonal NS. Figure SI-2d is a HRTEM image of a NS onto (110)SVO. The SVO film is visible in the top right corner of this image, while the  $\text{Sr}_3\text{V}_2\text{O}_8$  is visible in the remaining part of the image, with Moiré fringes. FFT of this area (figure SI-2e) displays reflections of both phases with the same orientations as on the EDP displayed on figure 3c. From these results, the elongation direction of the NS is determined as being [110].

Figures 3e,f give the EDPs of (111)SVO, showing the strong reflections of the perovskite phase together with weaker reflections due to the elongated NS. Tilting the sample allows to see three different variants of the  $\text{Sr}_3\text{V}_2\text{O}_8$  phase with the  $[5\bar{5}1]$  out-of-plane direction, and an epitaxial growth due again to the fact that the inter-planar distance  $d(110)$  of  $\text{Sr}_3\text{V}_2\text{O}_8$  is close to  $d(\bar{1}10)$  of SVO. Since along the [111] zone axis, this distance is equivalent to the  $d(01\bar{1})$  and  $d(10\bar{1})$  distances, this leads to the formation of three elongated variants rotated by  $60^\circ$  with respect to each other, as displayed in the AFM image (figure 1c). Figure 3g shows a scheme of the EDP with the reflections of the SVO film and those of one variant, while the figure 3h displays the scheme of the EDP with the three variants. The epitaxial relationships are:

$$[5\bar{5}1]\text{Sr}_3\text{V}_2\text{O}_8 // [111]\text{SVO}$$

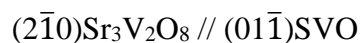
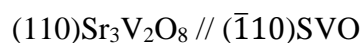
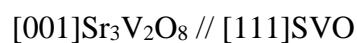
$$(\bar{1}\bar{1}0)\text{Sr}_3\text{V}_2\text{O}_8 // (\bar{1}10)\text{SVO}$$

$$(\bar{1}05)\text{Sr}_3\text{V}_2\text{O}_8 // (01\bar{1})\text{SVO}$$

The corresponding cell orientations are schematized on the figure 4c-II-elongated nanostructures. The mismatches between SVO and  $\text{Sr}_3\text{V}_2\text{O}_8$  are equal to -3.69 % for the first in-plane direction and -14.39 % for the second one.

In order to investigate the hexagonal NS, another area of the (111)SVO film grown on (111)STO was investigated as seen on figure 5. On the bright field image displayed on figure 5a, one can observe the triangular-shaped  $\text{Sr}_3\text{V}_2\text{O}_8$  crystallites which have a slightly darker contrast than the SVO matrix. Since the  $\text{Sr}_3\text{V}_2\text{O}_8$  phase possesses the rhombohedral symmetry, it comes from these crystallites have grown with the following relationships:  $[001]\text{Sr}_3\text{V}_2\text{O}_8$  (in hexagonal settings) // [111]SVO. Since the inter planar distances  $d(1\bar{1}0)\text{SVO} = 2.71 \text{ \AA}$  and

1  
2  
3  
4  
5  
6  
7  
8  
9  
10  
11  
12  
13  
14  
15  
16  
17  
18  
19  
20  
21  
22  
23  
24  
25  
26  
27  
28  
29  
30  
31  
32  
33  
34  
35  
36  
37  
38  
39  
40  
41  
42  
43  
44  
45  
46  
47  
48  
49  
50  
51  
52  
53  
54  
55  
56  
57  
58  
59  
60  
61  
62  
63  
64  
65  
d(110)Sr<sub>3</sub>V<sub>2</sub>O<sub>8</sub> = 2.81 Å are very close, the reflections of the orthovanadate are not visible on the corresponding EDP (figure 5b). These epitaxial relationships, schematized on figures 4c-I-triangular nanostructures, are:



The bright field image after tilting of the sample (figure 5c) shows dense Moiré fringes in the whole area indicating a large coverage of the triangular-shaped crystallites on the SVO film as evidenced by AFM (figure 1c). For this out-of-plane orientation, the mismatch between SVO and Sr<sub>3</sub>V<sub>2</sub>O<sub>8</sub> is equal to -3.69 % for the three equivalent in-plane directions. Concerning the elongated crystallites, some of them are visible on the bright field image displayed on figure 5d, with a dark contrast under some peculiar misorientations with respect to the zone axis. Since the lattice mismatch is similar for all the directions, this maybe explains why the elongated NS are less numerous (as they are anisotropic) than the triangular-shaped crystallites as it can be seen on figure 1c. Figure SI-2f is a HRTEM image of an elongated Sr<sub>3</sub>V<sub>2</sub>O<sub>8</sub> NS on (111)SVO. The superposition of the lattice of this NS onto the SVO film involves Moiré fringes on the image. FFT of the Sr<sub>3</sub>V<sub>2</sub>O<sub>8</sub> area shows additional reflections compared to the FFT of the SVO film alone (figure SI-2g) as observed on the EDP on figure 3e,f, with reflections due to the Moiré fringes. All these measurements have shown the different epitaxial relationships of the NS on the different orientations of the SVO matrix. As this SVO film can be tuned with different crystallographic directions, it results different configurations of the elongated NS: alignment along only one direction of all the NS for (110)SVO, NS orthogonal alignment with (100)SVO and finally 60° from each other with the (111)SVO. Furthermore for the (111)SVO another type of NS is stabilized with triangular shape due to strain effect.

In order to observe the different NS, fragment of SVO images have been investigated in bright and dark field for all the orientations (figure SI-3). These analyses confirm that the additional reflections observed in the EDPs are due to the NS.

From these crystallographic and epitaxial analyses, some elements can be given relative to the formation and growth of the Sr<sub>3</sub>V<sub>2</sub>O<sub>8</sub> nanostructures from the SVO matrix. Apparition of the nanostructures is a complex problem controlled by thermodynamic and kinetic driving forces<sup>44-46</sup>. The Sr<sub>3</sub>V<sub>2</sub>O<sub>8</sub> nanostructures are generated by a structural phase transformation from cubic SVO to rhombohedral Sr<sub>3</sub>V<sub>2</sub>O<sub>8</sub> due to oxidation of the vanadium, which seems more stable at

1 high temperature than the perovskite phase. The two phases SVO and  $\text{Sr}_3\text{V}_2\text{O}_8$  present strong  
2 differences: compare to SVO with 6 atoms/cell (cubic phase  $a = 3.86 \text{ \AA}$ ), the orthovanadate  
3  $\text{Sr}_3\text{V}_2\text{O}_8$  is a complex phase with 39 atoms/cell, with larger lattice constants ( $a = 5.62 \text{ \AA}$ ,  $c =$   
4  $20.1 \text{ \AA}$ ). In the diluted NS regime without coarsening, the energy  $E$  of a single NS is the sum  
5 of three contributions  $E_{\text{surf}}$  the surface energy,  $E_{\text{relax}}$  the elastic relaxation energy, and  $E_{\text{edges}}$  the  
6 short range contribution of edges. Even if the surface energies of  $\text{Sr}_3\text{V}_2\text{O}_8$  and SVO are not  
7 referenced to our knowledge, some statements can be done from comparative observation of  
8 NS formed in the same growth conditions.  
9

10  
11 In terms of relaxation energies, a summary of lattice misfits is given in table SI-1, and we  
12 observed in cases of elongated NS (for (100), (110) and (111) SVO matrices), that the longer  
13 direction is always  $[110]\text{Sr}_3\text{V}_2\text{O}_8$ . This is the direction where the compressive lattice mismatch  
14 is lower inducing elongated nanostructures<sup>45-47</sup>. Moreover, the orientations of the growth planes  
15 have been extracted from Fast Fourier Transform (FFT) of the TEM images: Figure SI\_2 a,b,c  
16 for 100(SVO) orientation, Figure SI\_2 d,e for 110(SVO) orientation and Figure SI\_2 f,g for  
17 (111)SVO orientation, and figure 5a-b for triangular nanostructures. The results have been  
18 summarized in the table SI-2 and figures SI-4,5,6.  
19

20  
21 It results that the growth plane (110) $\text{Sr}_3\text{V}_2\text{O}_8$  is present for all elongated nanostructures and we  
22 can qualitatively conclude that the surface energy of the (110) $\text{Sr}_3\text{V}_2\text{O}_8$  growth plane is lower  
23 than other contributions and drives NS elongation mechanism.  
24

25  
26 For the (111)SVO orientation, the two types of nanostructure are observed (elongated and  
27 triangular one). In this case, there is a competition between the influence of the lattice mismatch  
28 and the surface energy of the growth planes.  
29

30  
31 An exact interpretation of all NS types in term of thermodynamics, needs both: a  
32 complete study of the coarsening of each NS with their fine geometry; and mechanical  
33 coefficient of materials, and *ab initio* calculations of surface energies of both materials. We hope  
34 that our present NS panorama for each (100), (110), and (111)SVO films will stimulate such  
35 *ab initio* calculations.  
36  
37  
38  
39  
40  
41  
42  
43  
44  
45  
46  
47  
48  
49  
50  
51  
52  
53  
54  
55  
56  
57  
58  
59  
60  
61  
62  
63  
64  
65

## 2- Sr<sub>3</sub>V<sub>2</sub>O<sub>8</sub> nanostructures growth on a polycrystalline STO substrate

As observed in the study on the single crystalline substrates, the shape and the orientation of the NS depend on the crystalline orientation of the SVO matrix through complex epitaxial relationships. In order to explore the different types of NS available on more exotic matrix orientations, we have grown a SVO thin film on a CSE STO substrate, and observed the nanostructures on different grain orientations.

Prior to film deposition, EBSD has been performed on the polycrystalline STO substrate in order to determine the different orientations of the grains. Red, green and blue colours correspond to (100)STO, (110)STO and (111)STO orientations, (see figure SI-7a). Other colours as yellow, purple, pink etc. are attributed to higher index orientations determined by the stereographic orientation. The same area was again investigated by EBSD after the SVO deposition (see figure SI-7b). For the determination of the grain orientation, the same crystallographic phase was used for STO and SVO (space group  $Pm\bar{3}m$ ). As it can be seen, the same colour code of the individual grains is obtained after the SVO deposition, indicating a coherent growth. Nevertheless, the NS are too small to be detected by EBSD. Therefore, AFM measurements have been performed on several grains having the different crystallographic directions determined by EBSD (see figure 6). The same letter has been assigned to each analysed grain on the EBSD map and on the AFM images (see figures 6 and figures SI-8 to 10). According to the stereographic projection unit, the grains coloured in red, green and blue are (100), (110) and (111) preferentially oriented, respectively, and the corresponding AFM images (figure 6) show that the NS morphologies and in-plane orientations are similar to those observed on figure 1, as expected. Therefore, the CSE STO polycrystalline substrate presents the same characteristics than single crystalline substrates and promotes locally the same epitaxy.

The NS grown on (100)-oriented grains present the same morphology with in-plane 90° rotation relatively to each other in relation with the previously characterised epitaxial relationships. The difference in the in-plane rotation between each grain is related to the random orientation of the grains relatively to each other due to the polycrystalline nature of the CSE substrates. Nevertheless some NS size difference can also be observed depending on the individual grain although the same annealing time is simultaneously applied for all the grains. This effect could be attributed to small misorientations introducing miscuts on the surface which could modify the surface energy, the growth velocity and the shape of the NS compared to the single crystalline STO substrates. This statement is qualitatively supported by the small width of

1 terraces observed on figure SI-1. For growth on (110)-oriented grains, (in green in figure 6),  
2 the same elongated NS along a single direction are observed (figure SI-9). Finally, for growth  
3 on (111)-oriented grains (in blue in figure 6), the triangular shaped NS are mostly present  
4 (figure SI-10) as already observed on single crystal substrates (figure 1c).  
5  
6

7 AFM images of the grains c and d, that have preferential orientations lying in between (110)  
8 and (111) (figure 6), shows that the NS present also only one in-plane direction of elongation,  
9 as for the (110) orientation. Furthermore, the NS shape tends to be triangular, therefore both  
10 interesting features, i.e. a single orientation with triangular shaped NS, can be obtained from  
11 (110) and (111) orientations.  
12  
13

14 From (111) to (100) orientations, the density of the NS seems to decrease and a mixture of large  
15 and small NS are present (grains a and b on figure 6).  
16  
17

18 Finally, from (100) to (110) orientations, the NS shape can be tuned with a triangular shape and  
19 a flat surface, along with an increase of their density and size. Therefore, two interesting  
20 parameters seems to be crucial for the control of the NS: the epitaxial relationships and the  
21 lattice mismatch between the nanostructures and the matrix as determined by the TEM  
22 characterisations. This study on CSE STO substrates with intermediate orientations compared  
23 to high symmetry ones, shows that CSE can be a fast platform for testing thermodynamic and  
24 kinetic of nanostructures formation.  
25  
26  
27  
28  
29  
30  
31  
32  
33  
34  
35  
36  
37  
38  
39

### 40 **3. Dissolution of the nanostructures**

41 Figure 7 shows the AFM images of the films after water dissolution of NS for different substrate  
42 orientations. On single crystalline (100) and (110) STO substrates, clear imprint features are  
43 observed, associated to the previously presented NS that are half buried in the SVO matrix<sup>34,37</sup>.  
44 In case of the (111)STO substrate, the dissolution is incomplete with no clear evidence of  
45 imprints due to the presence of NS with their characteristic triangular form. Actually, an  
46 additional time of 30 s under water has been necessary to dissolve entirely the NS in this sample  
47 (figure SI-11) but still without clear imprints in the matrix. Only an elongated NS has left an  
48 imprint after dissolution as depicted by the red circle in figure SI-11. Therefore, the triangular  
49 shaped NS seem to grow on the surface of the SVO film, without the embedding in the matrix.  
50  
51  
52  
53  
54  
55  
56  
57  
58  
59  
60  
61  
62  
63  
64  
65

1 For comparison, the dissolution of NS has been performed also on the polycrystalline substrate.  
2 Some areas of interest have been selected and are displayed in the figure 7. As for the single  
3 crystalline (100) and (110)STO substrates, the same morphologies are obtained for oriented  
4 (100) and (110) grains. Moreover, dissolution of NS for the (111) orientation is not complete  
5 although all areas were equally rinsed with the same duration. Interestingly, the dissolution of  
6 such NS correspond to an intermediate area. New imprints are then observed on the surface. A  
7 simple way of preparing the surface of the SVO film to obtain imprint features of the NS in the  
8 SVO matrix is now reachable.  
9  
10  
11  
12  
13

## 14 CONCLUSIONS

15  
16  
17  
18  
19 Oxidation of SrVO<sub>3</sub> films leads to the growth of the orthovanadate Sr<sub>3</sub>V<sub>2</sub>O<sub>8</sub> phase in the form  
20 of NS, for which orientations depend on the orientation of the subjacent SrTiO<sub>3</sub> substrate.  
21 Complex epitaxial relationships were evidenced for all the observed NS variants, with different  
22 crystallites shapes according to the out-of-plane and in-plane orientations: (i) on (100)STO, the  
23 Sr<sub>3</sub>V<sub>2</sub>O<sub>8</sub> phase grows as elongated NS along the  $[\bar{5}52]$  out-of-plane direction with two  
24 equivalent variants forming a 90° angle; (ii) on (110)STO, the Sr<sub>3</sub>V<sub>2</sub>O<sub>8</sub> phase grows as  
25 elongated NS along the  $[5\bar{5}4]$  out-of-plane direction; (iii) on (111)STO, the Sr<sub>3</sub>V<sub>2</sub>O<sub>8</sub> phase  
26 grows as hexagonal-shaped crystallites along the  $[001]$  out-of-plane direction and also  
27 elongated NS along the  $[5\bar{5}1]$  out-of-plane direction (3 variants). Such particular shapes of the  
28 NS are closely related to the initial orientation of the substrate. Furthermore, we are showing  
29 that polycrystalline substrates are a powerful tool to investigate a large diversity of NS  
30 depending on the orientation of the SVO matrix and provides a fast way to establish a NS  
31 library. Dissolution of the NS have also been performed confirming that most of the NS are  
32 partially buried in the matrix and typical imprints features can be rapidly obtained by controlling  
33 the rinsing time. This work presents a first step to the elaboration and design of self-organized  
34 NS in order to prepare particular surfaces with specific designs for future integration of SVO  
35 or to extend its use to new applications.  
36  
37  
38  
39  
40  
41  
42  
43  
44  
45  
46  
47  
48  
49  
50  
51  
52  
53  
54  
55  
56  
57  
58  
59  
60  
61  
62  
63  
64  
65

1  
2 **Acknowledgements**  
3

4 The authors acknowledge the LabEx CHARMMMAT for financial support and the French  
5 Agence Nationale de la Recherche (ANR) (ANR-17-CE08-0012) in the framework of the  
6 POLYNASH project. TEM were performed on ScanMAT facilities platforms (UMS 2001,  
7 University of Rennes 1-CNRS). ISCR and ScanMAT received a financial support from the  
8 Region Bretagne, Rennes Metropole, the Departement d'Ille-et-Vilaine and the European Union  
9 (CPER-FEDER 2007–2014, Presage Nos. 39126 and 37339, and CPER 2015–2020  
10 MULTIMAT ScanMAT). We thank the Région Normandie for the PlaceNano RIN project.  
11  
12  
13  
14  
15  
16  
17  
18  
19  
20  
21  
22  
23  
24  
25  
26  
27  
28  
29  
30  
31  
32  
33  
34  
35  
36  
37  
38  
39  
40  
41  
42  
43  
44  
45  
46  
47  
48  
49  
50  
51  
52  
53  
54  
55  
56  
57  
58  
59  
60  
61  
62  
63  
64  
65

## References

- (1) Coll, M.; Fontcuberta, J.; Althammer, M.; Bibes, M.; Boschker, H.; Calleja, A.; Cheng, G.; Cuoco, M.; Dittmann, R.; Dkhil, B.; El Baggari, I.; Fanciulli, M.; Fina, I.; Fortunato, E.; Frontera, C.; Fujita, S.; Garcia, V.; Goennenwein, S. T. B.; Granqvist, C.-G.; Grollier, J.; Gross, R.; Hagfeldt, A.; Herranz, G.; Hono, K.; Houwman, E.; Huijben, M.; Kalaboukhov, A.; Keeble, D. J.; Koster, G.; Kourkoutis, L. F.; Levy, J.; Lira-Cantu, M.; MacManus-Driscoll, J. L.; Mannhart, J.; Martins, R.; Menzel, S.; Mikolajick, T.; Napari, M.; Nguyen, M. D.; Niklasson, G.; Paillard, C.; Panigrahi, S.; Rijnders, G.; Sánchez, F.; Sanchis, P.; Sanna, S.; Schlom, D. G.; Schroeder, U.; Shen, K. M.; Siemon, A.; Spreitzer, M.; Sukegawa, H.; Tamayo, R.; van den Brink, J.; Pryds, N.; Granozio, F. M. Towards Oxide Electronics: A Roadmap. *Appl Sur Sci* **2019**, *482*, 1–93. <https://doi.org/10.1016/j.apsusc.2019.03.312>.
- (2) Rao, C. N. R. The World of Perovskite Oxides: From Dielectrics to Superconductors. *Phys. C* **1988**, *153–155*, 1762–1768. [https://doi.org/10.1016/0921-4534\(88\)90470-4](https://doi.org/10.1016/0921-4534(88)90470-4).
- (3) Schlom, D. G.; Chen, L.-Q.; Pan, X.; Schmehl, A.; Zurbuchen, M. A. A Thin Film Approach to Engineering Functionality into Oxides. *J. Am. Ceram. Soc.* **2008**, *91* (8), 2429–2454. <https://doi.org/10.1111/j.1551-2916.2008.02556.x>.
- (4) Zubko, P.; Gariglio, S.; Gabay, M.; Ghosez, P.; Triscone, J.-M. Interface Physics in Complex Oxide Heterostructures. *Annu. Rev. Condens. Matter Phys.* **2011**, *2* (1), 141–165. <https://doi.org/10.1146/annurev-conmatphys-062910-140445>.
- (5) Moure, C.; Peña, O. Recent Advances in Perovskites: Processing and Properties. *Prog. Solid State Chem.* **2015**, *43* (4), 123–148. <https://doi.org/10.1016/j.progsolidstchem.2015.09.001>.
- (6) Chamberland, B. L.; Danielson, P. S. Alkaline-Earth Vanadium (IV) Oxides Having AVO<sub>3</sub> Composition. *J. Solid State Chem.* **1971**, *3* (2), 243-. [https://doi.org/10.1016/0022-4596\(71\)90035-1](https://doi.org/10.1016/0022-4596(71)90035-1).
- (7) Giannakopoulou, V.; Odier, P.; Bassat, J. M.; Loup, J. P. SrVO<sub>3</sub> and Sr<sub>2</sub>VO<sub>4</sub>, Electrical-Properties below and above Room-T. *Solid State Commun.* **1995**, *93* (7), 579–583. [https://doi.org/10.1016/0038-1098\(94\)00834-Y](https://doi.org/10.1016/0038-1098(94)00834-Y).
- (8) Moyer, J. A.; Eaton, C.; Engel-Herbert, R. Highly Conductive SrVO<sub>3</sub> as a Bottom Electrode for Functional Perovskite Oxides. *Adv. Mater.* **2013**, *25* (26), 3578–3582. <https://doi.org/10.1002/adma.201300900>.
- (9) Zhang, L.; Zhou, Y.; Guo, L.; Zhao, W.; Barnes, A.; Zhang, H.-T.; Eaton, C.; Zheng, Y.; Brahlek, M.; Haneef, H. F.; Podraza, N. J.; Chan, M. H. W.; Gopalan, V.; Rabe, K. M.; Engel-Herbert, R. Correlated Metals as Transparent Conductors. *Nat. Mater.* **2015**, *15* (2), 204–210. <https://doi.org/10.1038/nmat4493>.
- (10) Mirjolet, M.; Vasili, H. B.; López-Conesa, Ll.; Estradé, S.; Peiró, F.; Santiso, J.; Sánchez, F.; Machado, P.; Gargiani, P.; Valvidares, M.; Fontcuberta, J. Independent Tuning of Optical Transparency Window and Electrical Properties of Epitaxial SrVO<sub>3</sub> Thin Films by Substrate Mismatch. *Adv. Funct. Mater.* **2019**, *29* (37), 1904238. <https://doi.org/10.1002/adfm.201904238>.
- (11) Mirjolet, M.; Sánchez, F.; Fontcuberta, J. High Carrier Mobility, Electrical Conductivity, and Optical Transmittance in Epitaxial SrVO<sub>3</sub> Thin Films. *Adv. Funct. Mater.* **2019**, *29* (14), 1808432. <https://doi.org/10.1002/adfm.201808432>.
- (12) Boileau, A.; Cheikh, A.; Fouchet, A.; David, A.; Escobar-Galindo, R.; Labbé, C.; Marie, P.; Gourbilleau, F.; Lüders, U. Optical and Electrical Properties of the Transparent Conductor SrVO<sub>3</sub> without Long-Range Crystalline Order. *Appl. Phys. Lett.* **2018**, *112* (2), 021905. <https://doi.org/10.1063/1.5016245>.



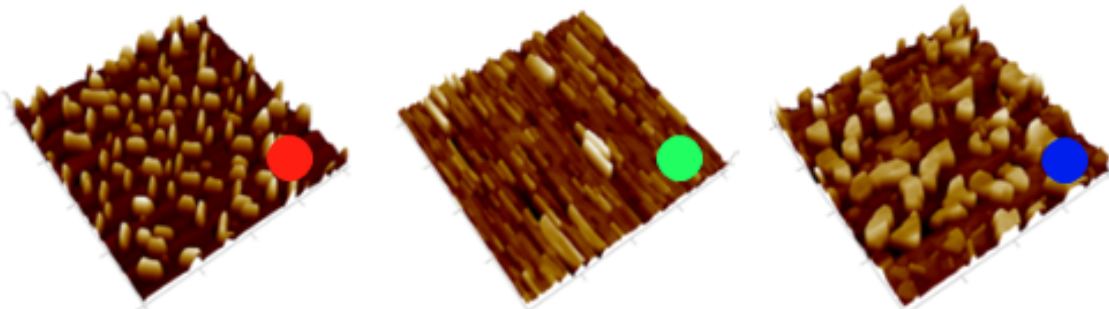
- 1  
2  
3  
4  
5  
6  
7  
8  
9  
10  
11  
12  
13  
14  
15  
16  
17  
18  
19  
20  
21  
22  
23  
24  
25  
26  
27  
28  
29  
30  
31  
32  
33  
34  
35  
36  
37  
38  
39  
40  
41  
42  
43  
44  
45  
46  
47  
48  
49  
50  
51  
52  
53  
54  
55  
56  
57  
58  
59  
60  
61  
62  
63  
64  
65
- (13) Boileau, A.; Cheikh, A.; Fouchet, A.; David, A.; Labbé, C.; Marie, P.; Gourbilleau, F.; Lüders, U. Tuning of the Optical Properties of the Transparent Conducting Oxide SrVO<sub>3</sub> by Electronic Correlations. *Adv. Opt. Mater.* **2019**, *7* (7), 1801516. <https://doi.org/10.1002/adom.201801516>.
  - (14) Megaw, H. D. Crystal Structure of Double Oxides of the Perovskite Type. *Proc. Phys. Soc. Lond.* **1946**, *58* (326), 133-. <https://doi.org/10.1088/0959-5309/58/2/301>.
  - (15) Range, K.; Rau, F.; Klement, U. High-Pressure Synthesis and Structure Refinement of SrVO<sub>3</sub>, Sr<sub>2</sub>VO<sub>4</sub>, and Sr<sub>3</sub>V<sub>2</sub>O<sub>7</sub>. *Z. Naturforschung Sect. B- J. Chem. Sci.* **1991**, *46* (10), 1315–1318.
  - (16) Rey, M.; Dehaut, P.; Joubert, J.; Lambertandron, B.; Cyrot, M.; Cyrot-Lackmann, F. Preparation and Structure of the Compounds SrVO<sub>3</sub> and Sr<sub>2</sub>VO<sub>4</sub>. *J. Solid State Chem.* **1990**, *86* (1), 101–108. [https://doi.org/10.1016/0022-4596\(90\)90119-I](https://doi.org/10.1016/0022-4596(90)90119-I).
  - (17) Garcia-Jaca, J.; Mesa, J. L.; Insausti, M.; Larramendi, J. I. R.; Arriortua, M. I.; Rojo, T. Synthesis, Crystal Structure, Stoichiometry and Magnetic Properties of (Ca<sub>1-x</sub>Sr<sub>x</sub>)VO<sub>3</sub>. *Mater. Res. Bull.* **1999**, *34* (2), 289–301. [https://doi.org/10.1016/S0025-5408\(99\)00002-1](https://doi.org/10.1016/S0025-5408(99)00002-1).
  - (18) Dougier, P.; Fan, J.; Goodenough, J. Study of Magnetic, Electrical and Optical-Properties of Phases of Perovskite Structure SrVO<sub>2.90</sub> and SrVO<sub>3</sub>. *J. Solid State Chem.* **1975**, *14* (3), 247–259. [https://doi.org/10.1016/0022-4596\(75\)90029-8](https://doi.org/10.1016/0022-4596(75)90029-8).
  - (19) Li, J.; Yin, D.; Li, Q.; Sun, R.; Huang, S.; Meng, F. Interfacial Defects Induced Electronic Property Transformation at Perovskite SrVO<sub>3</sub>/SrTiO<sub>3</sub> and LaCrO<sub>3</sub>/SrTiO<sub>3</sub> Heterointerfaces. *Phys. Chem. Chem. Phys.* **2017**, *19* (10), 6945–6951. <https://doi.org/10.1039/c6cp07691b>.
  - (20) Kim, D. W.; Kim, D. H.; Noh, T. W.; Char, K.; Park, J. H.; Lee, K. B.; Kim, H. D. Interface Chemistry and Electrical Properties of SrVO<sub>3</sub>/LaAlO<sub>3</sub> Heterostructures. *J. Appl. Phys.* **2000**, *88* (12), 7056–7059. <https://doi.org/10.1063/1.1326896>.
  - (21) Fouchet, A.; Rault, J. E.; Allain, M.; Berini, B.; Rueff, J.-P.; Dumont, Y.; Keller, N. Interface Chemical and Electronic Properties of LaAlO<sub>3</sub>/SrVO<sub>3</sub> Heterostructures. *J. Appl. Phys.* **2018**, *123* (5), 055302. <https://doi.org/10.1063/1.4998004>.
  - (22) Bourlier, Y.; Berini, B.; Fregnaux, M.; Fouchet, A.; Aureau, D.; Dumont, Y. Transfer of Epitaxial SrTiO<sub>3</sub> Nanothick Layers Using Water-Soluble Sacrificial Perovskite Oxides. *Acs Appl. Mater. Interfaces* **2020**, *12* (7), 8466–8474. <https://doi.org/10.1021/acsami.9b21047>.
  - (23) Berini, B.; Demange, V.; Bouttemy, M.; Popova, E.; Keller, N.; Dumont, Y.; Fouchet, A. Control of High Quality SrVO<sub>3</sub> Electrode in Oxidizing Atmosphere. *Adv. Mater. Interfaces* **2016**, *3* (18), 1600274. <https://doi.org/10.1002/admi.201600274>.
  - (24) Germanicus, R. C.; Bourlier, Y.; Notot, V.; Bérini, B.; Demange, V.; Berthe, M.; Boileau, A.; Euchin, M.; Dumont, Y.; Aureau, D.; Fregnaux, M.; Grandidier, B.; Lüders, U.; David, A.; Prellier, W.; Biadala, L.; Fouchet, A. Three Dimensional Resistance Mapping of Self-Organized Sr<sub>3</sub>V<sub>2</sub>O<sub>8</sub> Nanorods on Metallic Perovskite SrVO<sub>3</sub> Matrix. *Appl. Surf. Sci.* **2020**, *510*, 145522. <https://doi.org/10.1016/j.apsusc.2020.145522>.
  - (25) Yaremchenko, A. A.; Brinkmann, B.; Janssen, R.; Frade, J. R. Electrical Conductivity, Thermal Expansion and Stability of Y- and Al-Substituted SrVO<sub>3</sub> as Prospective SOFC Anode Material. *Solid State Ion.* **2013**, *247*, 86–93. <https://doi.org/10.1016/j.ssi.2013.06.002>.
  - (26) Macias, J.; Yaremchenko, A. A.; Frade, J. R. Redox Transitions in Strontium Vanadates: Electrical Conductivity and Dimensional Changes. *J. Alloys Compd.* **2014**, *601*, 186–194. <https://doi.org/10.1016/j.jallcom.2014.02.148>.

- 1  
2  
3  
4  
5  
6  
7  
8  
9  
10  
11  
12  
13  
14  
15  
16  
17  
18  
19  
20  
21  
22  
23  
24  
25  
26  
27  
28  
29  
30  
31  
32  
33  
34  
35  
36  
37  
38  
39  
40  
41  
42  
43  
44  
45  
46  
47  
48  
49  
50  
51  
52  
53  
54  
55  
56  
57  
58  
59  
60  
61  
62  
63  
64  
65
- (27) Bourlier, Y.; Frégnaux, M.; Bérini, B.; Fouchet, A.; Dumont, Y.; Aureau, D. Surface Characterizations and Selective Etching of Sr-Rich Segregation on Top of SrVO<sub>3</sub> Thin-Films Grown by Pulsed Laser Deposition. *ChemNanoMat* **2019**, *5* (5), 674–681. <https://doi.org/10.1002/cnma.201900017>.
- (28) Han, Z. W.; Wang, Z.; Feng, X. M.; Li, B.; Mu, Z. Z.; Zhang, J. Q.; Niu, S. C.; Ren, L. Q. Antireflective Surface Inspired from Biology: A Review. *Biosurface Biotribology* **2016**, *2* (4), 137–150. <https://doi.org/10.1016/j.bsbt.2016.11.002>.
- (29) Dey, P.; Saha, S. K.; Chakraborty, S. Surface Nanostructure–Wettability Coupling Leads to Unique Topological Evolution Dictating Water Transport over Nanometer Scales. *Langmuir* **2020**, *36* (28), 8111–8122. <https://doi.org/10.1021/acs.langmuir.0c00955>.
- (30) Lacotte, M.; David, A.; Pravarthana, D.; Grygiel, C.; Rohrer, G. S.; Salvador, P. A.; Velazquez, M.; de Kloe, R.; Prellier, W. Growth of Ca<sub>2</sub>MnO<sub>4</sub> Ruddlesden-Popper Structured Thin Films Using Combinatorial Substrate Epitaxy. *J. Appl. Phys.* **2014**, *116* (24), 245303. <https://doi.org/10.1063/1.4905012>.
- (31) Lacotte, M.; David, A.; Rohrer, G. S.; Salvador, P. A.; Prellier, W. Preferential Orientation Relationships in Ca<sub>2</sub>MnO<sub>4</sub> Ruddlesden-Popper Thin Films. *J. Appl. Phys.* **2015**, *118* (4), 045306. <https://doi.org/10.1063/1.4927518>.
- (32) Pravarthana, D.; Lebedev, O. I.; Hebert, S.; Chateigner, D.; Salvador, P. A.; Prellier, W. High-Throughput Synthesis of Thermoelectric Ca<sub>3</sub>Co<sub>4</sub>O<sub>9</sub> Films. *Appl. Phys. Lett.* **2013**, *103* (14), 143123. <https://doi.org/10.1063/1.4824212>.
- (33) Pravarthana, D.; Chateigner, D.; Lutterotti, L.; Lacotte, M.; Marinel, S.; Dubos, P. A.; Hervas, I.; Hug, E.; Salvador, P. A.; Prellier, W. Growth and Texture of Spark Plasma Sintered Al<sub>2</sub>O<sub>3</sub> Ceramics: A Combined Analysis of X-Rays and Electron Back Scatter Diffraction. *J. Appl. Phys.* **2013**, *113* (15), 153510. <https://doi.org/10.1063/1.4802439>.
- (34) Pravarthana, D.; Trassin, M.; Chu, J. H.; Lacotte, M.; David, A.; Ramesh, R.; Salvador, P. A.; Prellier, W. BiFeO<sub>3</sub>/La<sub>0.7</sub>Sr<sub>0.3</sub>MnO<sub>3</sub> Heterostructures Deposited on Spark Plasma Sintered LaAlO<sub>3</sub> Substrates. *Appl. Phys. Lett.* **2014**, *104* (8), 082914. <https://doi.org/10.1063/1.4867021>.
- (35) Pravarthana, D.; Lebedev, O. I.; David, A.; Fouchet, A.; Trassin, M.; Rohrer, G. S.; Salvador, P. A.; Prellier, W. Metastable Monoclinic [110] Layered Perovskite Dy<sub>2</sub>Ti<sub>2</sub>O<sub>7</sub> Thin Films for Ferroelectric Applications. *RSC Adv.* **2019**, *9* (35), 19895–19904. <https://doi.org/10.1039/C9RA04554F>.
- (36) Woo, S.; Jeong, H.; Lee, S. A.; Seo, H.; Lacotte, M.; David, A.; Kim, H. Y.; Prellier, W.; Kim, Y.; Choi, W. S. Surface Properties of Atomically Flat Poly-Crystalline SrTiO<sub>3</sub>. *Sci. Rep.* **2015**, *5* (1), 8822. <https://doi.org/10.1038/srep08822>.
- (37) Woo, S.; Lee, S. A.; Mun, H.; Choi, Y. G.; Zhung, C. J.; Shin, S.; Lacotte, M.; David, A.; Prellier, W.; Park, T.; Kang, W. N.; Lee, J. S.; Kim, S. W.; Choi, W. S. Enhanced Magnetic and Thermoelectric Properties in Epitaxial Polycrystalline SrRuO<sub>3</sub> Thin Films. *Nanoscale* **2018**, *10* (9), 4377–4384. <https://doi.org/10.1039/C7NR09627E>.
- (38) Pravarthana, D.; Lebedev, O. I.; Hebert, S.; Chateigner, D.; Salvador, P. A.; Prellier, W. High-Throughput Synthesis of Thermoelectric Ca<sub>3</sub>Co<sub>4</sub>O<sub>9</sub> Films. *Appl. Phys. Lett.* **2013**, *103* (14), 143123. <https://doi.org/10.1063/1.4824212>.
- (39) Pravarthana, D.; Chateigner, D.; Lutterotti, L.; Lacotte, M.; Marinel, S.; Dubos, P. A.; Hervas, I.; Hug, E.; Salvador, P. A.; Prellier, W. Growth and Texture of Spark Plasma Sintered Al<sub>2</sub>O<sub>3</sub> Ceramics: A Combined Analysis of X-Rays and Electron Back Scatter Diffraction. *J. Appl. Phys.* **2013**, *113* (15), 153510. <https://doi.org/10.1063/1.4802439>.
- (40) Dhanapal, P.; Guo, S.; Wang, B.; Yang, H.; Agarwal, S.; Zhan, Q.; Li, R.-W. High-Throughput Investigation of Orientations Effect on Nanoscale Magnetization Reversal

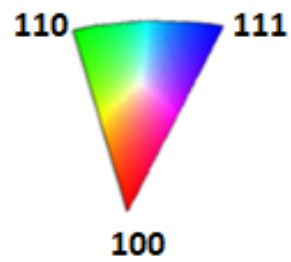
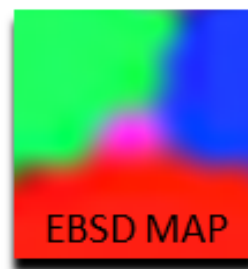
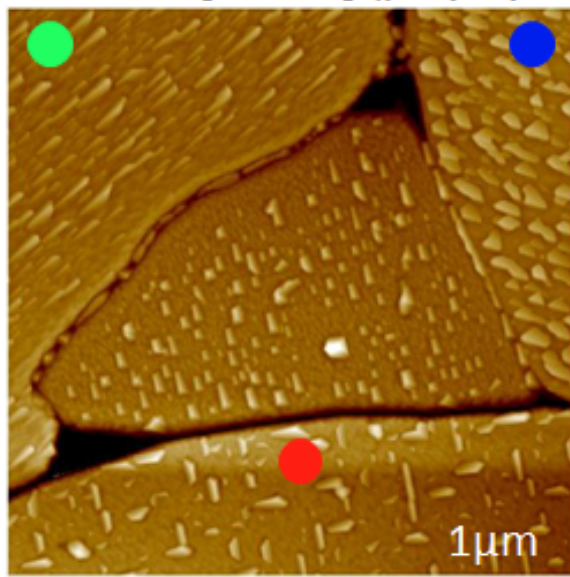
- 1  
2  
3  
4  
5  
6  
7  
8  
9  
10  
11  
12  
13  
14  
15  
16  
17  
18  
19  
20  
21  
22  
23  
24  
25  
26  
27  
28  
29  
30  
31  
32  
33  
34  
35  
36  
37  
38  
39  
40  
41  
42  
43  
44  
45  
46  
47  
48  
49  
50  
51  
52  
53  
54  
55  
56  
57  
58  
59  
60  
61  
62  
63  
64  
65
- in Cobalt Ferrite Thin Films Induced by Electric Field. *Appl. Phys. Lett.* **2017**, *111* (16), 162401. <https://doi.org/10.1063/1.4996375>.
- (41) Demange, V.; Bérini, B.; Gautier, B.; Popova, E.; Dumont, Y.; Fouchet, A. Ca<sub>3</sub>(VO<sub>4</sub>)<sub>2</sub> Nanowires on Metallic CaVO<sub>3</sub> Films as Nanocapacitors. *ACS Appl. Nano Mater.* **2020**, *3* (7), 6684–6692. <https://doi.org/10.1021/acsnm.0c01136>.
- (42) Eaton, C.; Moyer, J. A.; Alipour, H. M.; Grimley, E. D.; Brahlek, M.; LeBeau, J. M.; Engel-Herbert, R. Growth of SrVO<sub>3</sub> Thin Films by Hybrid Molecular Beam Epitaxy. *J. Vac. Sci. Technol. A* **2015**, *33* (6), 061504. <https://doi.org/10.1116/1.4927439>.
- (43) P. Hirsch, A. Howie, R. Nicholson, D. W. Pashley and M. J. Whelan. *Electron Microscopy of Thin Crystals*; Butterworths/Krieger, London/Malabar FL, 1965.
- (44) Gibert, M.; García, A.; Puig, T.; Obradors, X. Thermodynamic Stability Analysis of Isometric and Elongated Epitaxial Ce<sub>1-x</sub>Gd<sub>x</sub>O<sub>2-y</sub> Nanostructures on Perovskite Substrates. *Phys. Rev. B* **2010**, *82* (16), 165415. <https://doi.org/10.1103/PhysRevB.82.165415>.
- (45) Obradors, X.; Puig, T.; Gibert, M.; Queraltó, A.; Zabaleta, J.; Mestres, N. Chemical Solution Route to Self-Assembled Epitaxial Oxide Nanostructures. *Chem. Soc. Rev.* **2014**, *43* (7), 2200–2225. <https://doi.org/10.1039/C3CS60365B>.
- (46) Gibert, M.; Abellán, P.; Benedetti, A.; Puig, T.; Sandiumenge, F.; García, A.; Obradors, X. Self-Organized Ce<sub>1-x</sub>Gd<sub>x</sub>O<sub>2-y</sub> Nanowire Networks with Very Fast Coarsening Driven by Attractive Elastic Interactions. *Small* **2010**, *6* (23), 2716–2724. <https://doi.org/10.1002/sml.201001237>.
- (47) Queraltó, A.; De la Mata, M.; Arbiol, J.; Hühne, R.; Obradors, X.; Puig, T. Unveiling the Nucleation and Coarsening Mechanisms of Solution-Derived Self-Assembled Epitaxial Ce<sub>0.9</sub>Gd<sub>0.1</sub>O<sub>2-y</sub> Nanostructures. *Cryst. Growth Des.* **2017**, *17*, 504–516. <https://doi.org/10.1021/acs.cgd.6b01358>.

1  
2  
3  
4  
5  
6  
7  
8  
9  
10  
11  
12  
13  
14  
15  
16  
17  
18  
19  
20  
21  
22  
23  
24  
25  
26  
27  
28  
29  
30  
31  
32  
33  
34  
35  
36  
37  
38  
39  
40  
41  
42  
43  
44  
45  
46  
47  
48  
49  
50  
51  
52  
53  
54  
55  
56  
57  
58  
59  
60  
61  
62  
63  
64  
65

SrVO<sub>3</sub>/SrTiO<sub>3</sub> (single crystalline substrate)



SrVO<sub>3</sub>/SrTiO<sub>3</sub> (polycrystalline substrate)



**Self-organized Sr<sub>3</sub>V<sub>2</sub>O<sub>8</sub> nanostructures on SrVO<sub>3</sub> thin film**

Graphical abstract

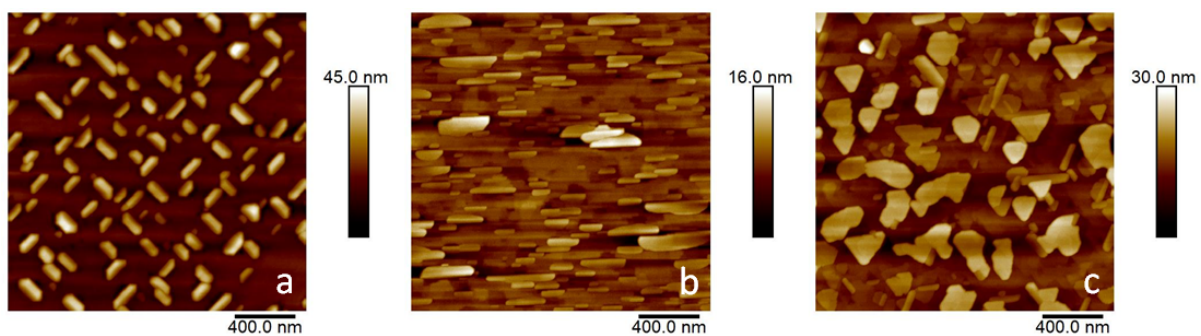


**Figure 1.** AFM images of the surface of a SVO film grown on three single crystalline STO substrates with the following orientations: a) (100), b) (110), and c) (111).  $Sr_3V_2O_8$  NS are observed with different shapes and sizes.

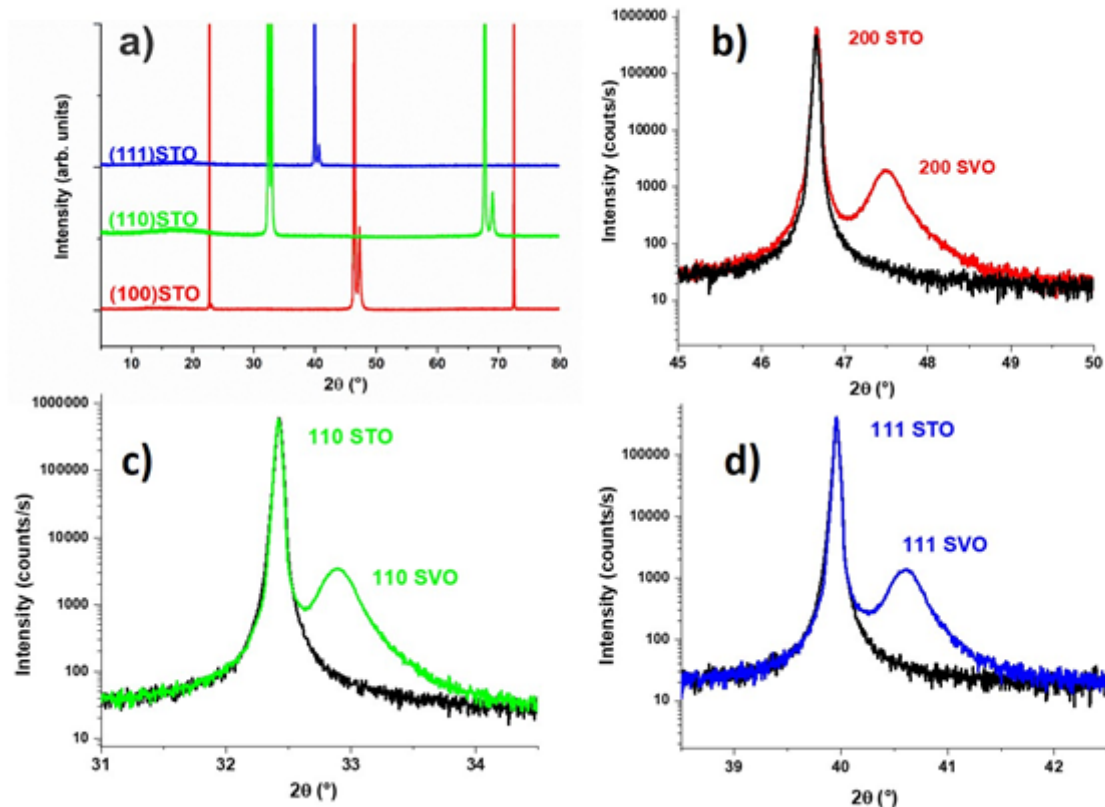


**Figure 2.** XRD patterns of the SVO films grown on various substrates: (a) full angular range pattern of films grown on (100)-, (110)- and (111)STO. b) Pattern of film grown on (100)STO around the (200) reflection (log. scale). c) Pattern of film grown on (110)STO around the (110) reflection (log. scale). d) Pattern of film grown on (111)STO around the (111) reflection (log. scale). A color code is adopted from EBSD where red line corresponds to SVO onto (100)STO, green line for (110)STO and blue line for (111)STO. For b,c,d, in black is the reference substrate without film.

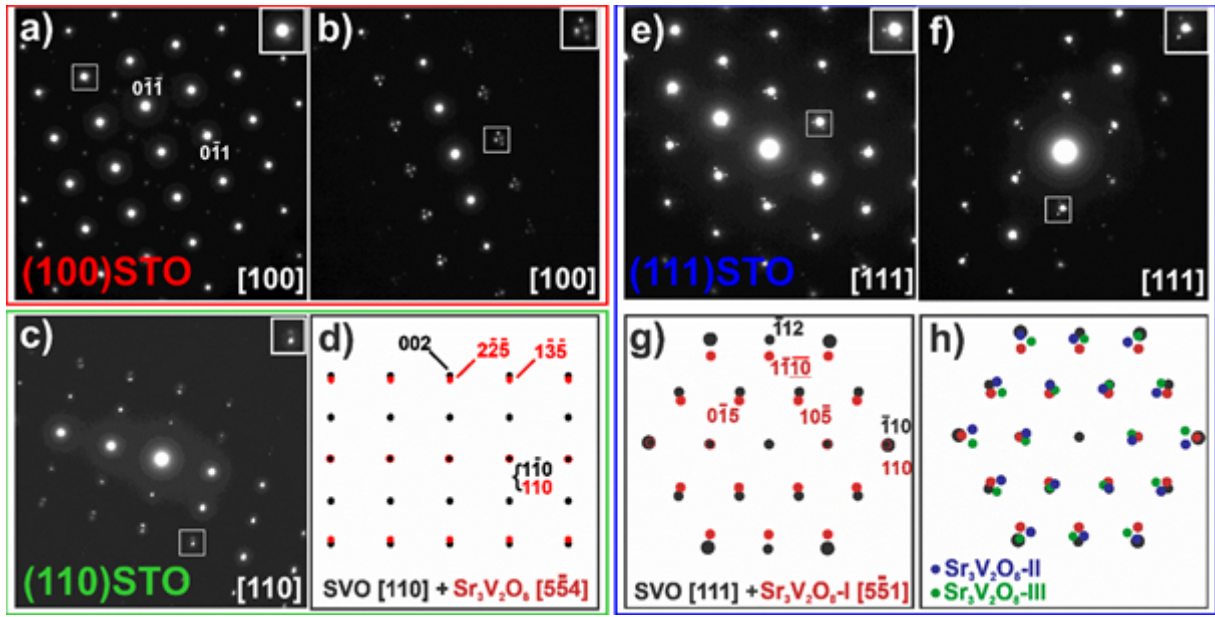


**Figure 3.** EDPs along the  $[100]$  zone axis (a) and slightly tilted from the zone axis (b) of the  $(100)$ SVO film displaying additional  $Sr_3V_2O_8$  NS weak reflections close to the strong SVO reflections, magnified in the insets. c) EDP slightly tilted from the  $[110]$ SVO zone. d) Scheme of the experimental EDP: reflections and labels of the SVO phase are displayed in black, those of the  $Sr_3V_2O_8$  phase are displayed in red. e),f) EDPs of the SVO films slightly tilted from the  $[111]$ SVO zone axis, showing three series of weak reflections due to the  $Sr_3V_2O_8$  NS oriented along the  $[5\bar{5}1]$  out-of-plane direction. g) Scheme of the EDP of the SVO film with reflections of one  $Sr_3V_2O_8$  variant (black: SVO; red: first variant the  $Sr_3V_2O_8$  of phase). h) Same with reflections of the three  $Sr_3V_2O_8$  variants (black: SVO; red, green, blue: the 3  $Sr_3V_2O_8$  variants).



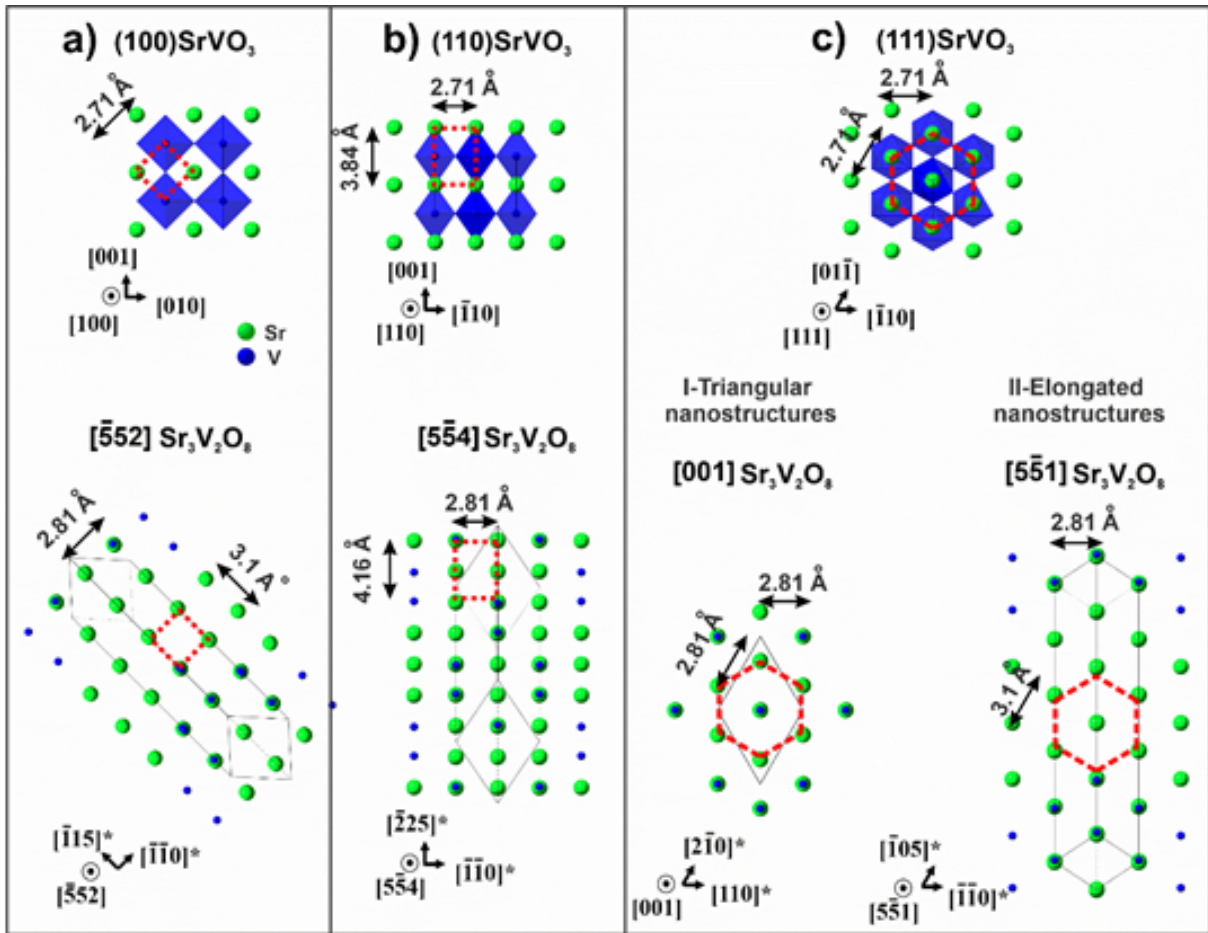


**Figure 4.** a) Schemes of the epitaxial relationships between the SVO phase (top part) and the Sr<sub>3</sub>V<sub>2</sub>O<sub>8</sub> phase (bottom part) on 100(STO) (a), (110)STO (b) and (111)STO (c). The in-plane coincidence cell for both phases is defined by dashed red lines for each orientation.



1  
2  
3  
4  
5  
6  
7  
8  
9  
10  
11  
12  
13  
14  
15  
16  
17  
18  
19  
20  
21  
22  
23  
24  
25  
26  
27  
28  
29  
30  
31  
32  
33  
34  
35  
36  
37  
38  
39  
40  
41  
42  
43  
44  
45  
46  
47  
48  
49  
50  
51  
52  
53  
54  
55  
56  
57  
58  
59  
60  
61  
62  
63  
64  
65

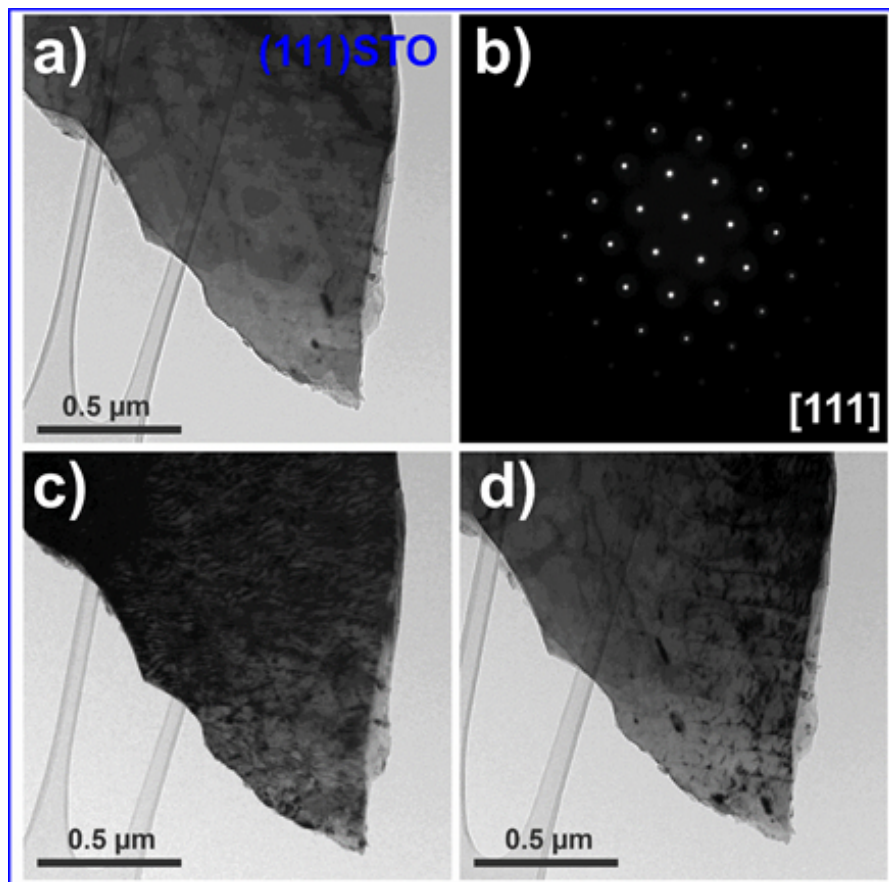


**Figure 5.** *a) Bright field image of a fragment of the SVO film grown on (111)STO. b) EDP along the [111] zone axis of SVO. c) Bright field of the same area slightly tilted and showing Moiré fringes. d) Same with another tilt allowing to see the elongated  $Sr_3V_2O_8$  NS.*

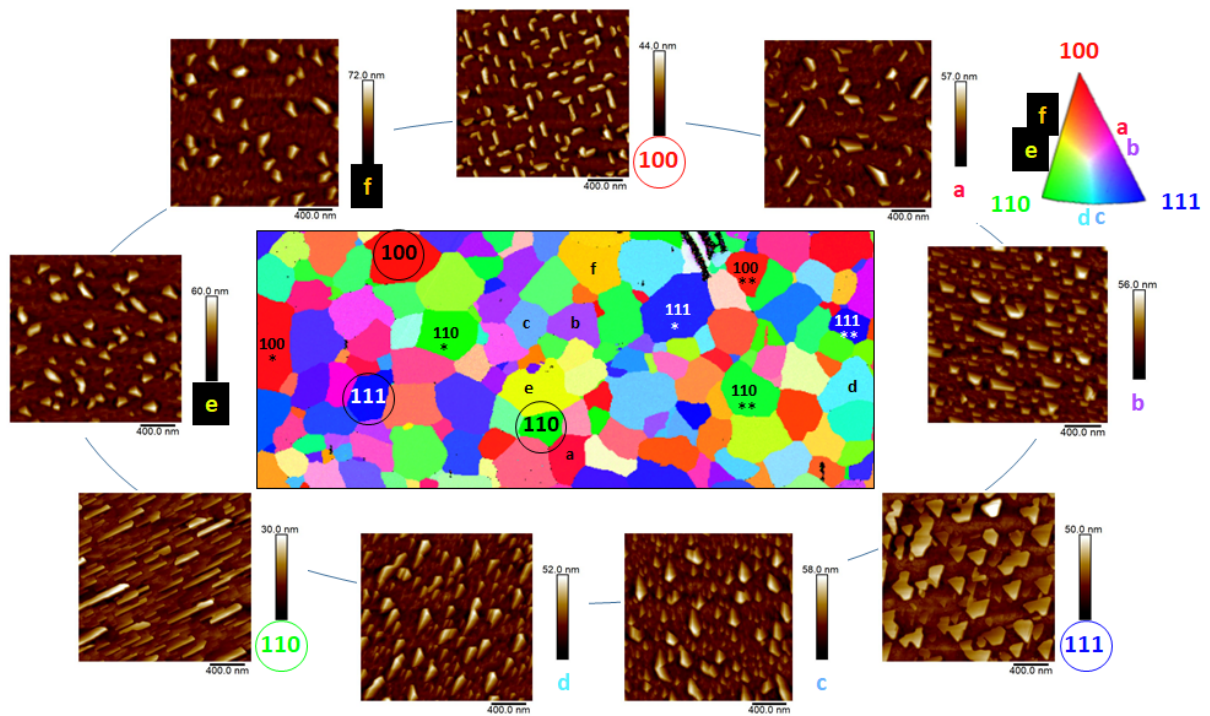


**Figure 6.** AFM images of selected grains of the SVO film onto the polycrystalline substrate having preferential (100), (110) and (111) out-of-plane orientations and intermediate orientations.

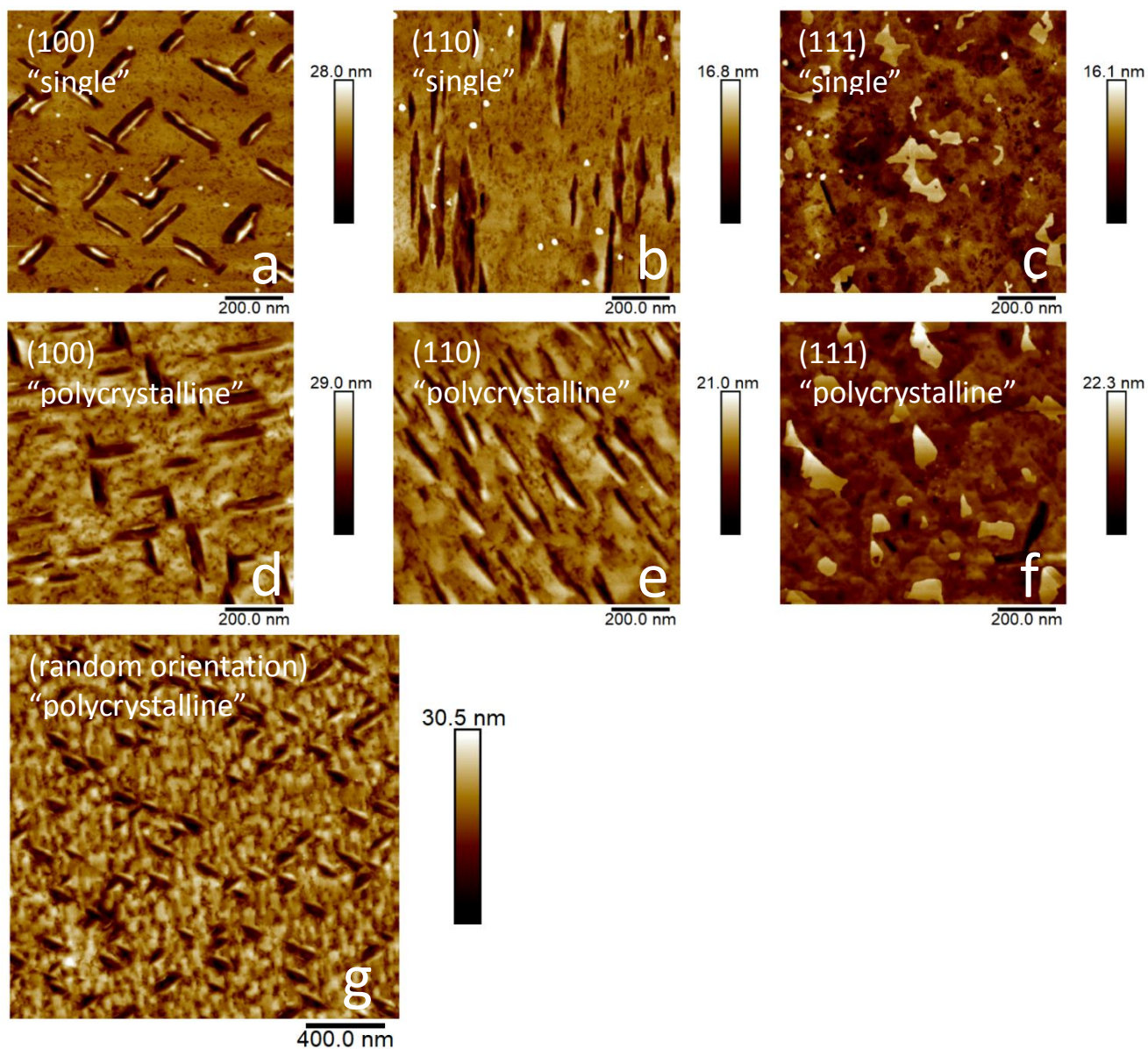
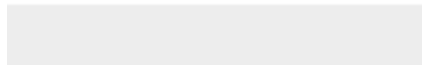


**Figure 7.** In first row, are presented AFM images of SVO films grown onto (100), (110) and (111)STO single crystalline substrates after dissolution of the NS (a), (b), (c) respectively and in second row, onto the polycrystalline substrate after dissolution of the NS for the three standard orientations (100), (100) and (111), (d), (e), (f), respectively. The last image (g) corresponds to a non-conventional orientation (yellow colored grain noted e in figure 6 as observed in EBSD map).



[Click here to access/download](#)

**Supplementary Material for on-line publication only**  
SI-revised bb-VD.docx



### Author contributions

B.B. and A.F. conceived and designed the experiments. B.B. synthesized the films by PLD and M.D. synthesized CSE substrates. V.D. and L.R. performed XRD and TEM measurements and analyzed all the measurements. B.B. performed AFM characterizations and analyzed with R.C.G. all AFM measurements. M.D. performed and analyzed with A.D. EBSD measurements. Y.B. performed the electrical transport measurements and analyzed with Y.D. the results. W.P., U.L., Y.D. have leadership responsibilities. B.B., M.D, V.D. and A.F. wrote the original manuscript with inputs from all authors.